analytical chemistry
Article
Cite This: *Anal. Chem.* 2018, 90, 5179−5186
pubs.acs.org/ac

Depth Profiling and Cross-Sectional Laser Ablation Ionization Mass Spectrometry Studies of Through-Silicon-Vias

Valentine Grimaudo,*,[†] Pavel Moreno-García,[†] Alena Cedeño López,[†] Andreas Riedo,[‡] Reto Wiesendanger,[§] Marek Tulej,[§] Cynthia Gruber,[∥] Emanuel Lörtscher,[∥] Peter Wurz,[§] and Peter Broekmann*,[†]

[†]Department of Chemistry and Biochemistry, University of Bern, Freiestrasse 3, 3012 Bern, Switzerland
[‡]Sackler Laboratory for Astrophysics, Leiden University, Niels Bohrweg 2, 2333 CA Leiden, The Netherlands
[§]Physics Institute, Space Research and Planetary Sciences, University of Bern, Sidlerstrasse 5, 3012 Bern, Switzerland
[∥]IBM Research - Zürich, Science and Technology Department, Säumerstrasse 4, 8803 Rüschlikon, Switzerland

Supporting Information

ABSTRACT: Through-silicon-via (TSV) technology enables 3D integration of multiple 2D components in advanced microchip architectures. Key in the TSV fabrication is an additive-assisted Cu electroplating process in which the additives employed may get embedded in the TSV body. This incorporation negatively influences the reliability and durability of the Cu interconnects. Here, we present a novel approach toward the chemical analysis of TSVs which is based on femtosecond laser ablation ionization mass spectrometry (fs-LIMS). The conditions for LIMS depth profiling were identified by a systematic variation of the laser pulse energy and the number of laser shots applied. In this contribution, new aspects are addressed related to the analysis of highly heterogeneous specimens having dimensions in the range of the probing beam itself. Particularly challenging were the different chemical and physical properties of which the target specimens were composed. Depth profiling of the TSVs along their main axis (approach 1) revealed a gradient in the carbon (C) content. These differences in the C concentration inside the TSVs could be confirmed and quantified by LIMS analyses of cross-sectionally sliced TSVs (approach 2). Our quantitative analysis revealed a C content that is ~1.5 times higher at the TSV top surface compared to its bottom. Complementary Scanning Auger Microscopy (SAM) data confirmed a preferential embedment of suppressor additives at the side walls of the TSV. These results demonstrate that the TSV filling concept significantly deviates from common Damascene electroplating processes and will therefore contribute to a more comprehensive, mechanistic understanding of the underlying mechanisms.

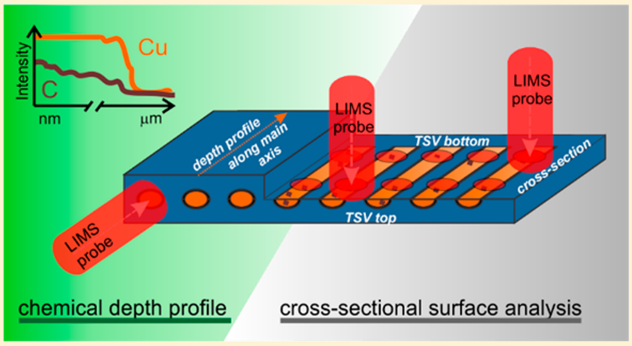

The striving to ever increase the performance of electronic devices has pushed the semiconductor industry close to the fundamental physical limitation of the CMOS (complementary metal-oxide-semiconductor) technology. The fading of Moore's law—which predicts a doubling of the transistor area density in a single processor unit every 18 to 24 months—indicates that both technical but also economical constraints are impeding. Past improvements in microprocessor performance were mainly achieved by miniaturization of the integrated circuits (IC).[1] However, further downscaling of the transistor technology is technically demanding and therefore economically less attractive as novel processing tools are required for every new generation.[2] This is the reason why much attention is currently being paid to novel scaling concepts which are based on the three-dimensional (3D) integration of individual 2D logic, memory, or hybrid layers. So far, a variety of technical concepts have been proposed ranging from wire-bonded stacking of individual dies (3D packing/3D-P), 3D wafer level packaging (3D WLP), to 3D stacking of circuits and individual transistor layers (3D-IC).[3] A key feature of the latter two approaches is the interconnection of individual functional 2D layers by means of insulated electrical connections, so-called through-silicon-vias (TSVs). These micrometer (μm)-sized Cu interconnects penetrate through the entire Si substrate to reach the next circuit layer.[4] Such TSV technology will allow for the vertical integration of multiple layers with minimal interconnection lengths thus enabling higher function densities and operational speed due to reduced signal loss and latency.[5,6] Besides the general issue of handling heat dissipation in such densely packed 3D structures without the possibility of a direct heat-sink attached, manufacturability, fabrication costs, and specific failure modes of TSV interconnects have so far

Received: December 19, 2017
Accepted: March 13, 2018
Published: March 26, 2018

DOI: 10.1021/acs.analchem.7b05313
Anal. Chem. 2018, 90, 5179−5186

prevented the widespread implementation of TSV technology in current microelectronic processing.[6] A major challenge is the achievement of defect-free filling along the entire length of a TSV with copper (Cu) by means of an additive-assisted electrochemical deposition (ECD) process to increase conductance of the TSV and reduce strain. Particularly challenging for the filling of TSVs is their extraordinarily large diameter-to-depth aspect ratio (up to 1/15)[6] to achieve deepest TSVs that penetrate optimally the entire wafer while consuming as little space as possible on it. So far, several TSV plating concepts have been discussed in the literature.[6−9] A more advanced TSV plating concept is based on a suppressor film gradient formation along the TSV side walls in the initial stage of the plating process. An important characteristic of this additive concept is the extraordinarily high robustness of the suppressing polymer films at the feature side walls which need to maintain their suppressing capabilities on the time scale of minutes during the entire TSV filling process. A possible and undesired side effect of this TSV plating concept is, however, the local embedment of these polymeric suppressor films at the feature side walls, which gets overgrown by the electrodeposited Cu in the course of the bottom-up filling process. On the other hand, the interior of the Cu TSV is expected to remain largely contamination free. As an example, Figure 1 shows a series of TSV features that were cross-sectioned by focused ion beam (FIB) milling prior to their SEM analysis. To characterize the performance and the mechanism of the underlying electrodeposition process, the bottom-up fill was stopped at different fill levels achieved at different plating times. Both the characteristic shape of the Cu growth front and the overburden "bump" formation (momentum plating) in the final stage of the filling process indicate a perfect bottom-up fill process. A uniform recrystallization (large recrystallized Cu grains) of the electrodeposited Cu inside the TSV is supportive for the absence of a distinct impurity concentration gradient along the interior of the structure.[10,11] Note that no extra thermal annealing treatment was applied to the displayed TSV structures. Fast recrystallization takes place already at room temperature (RT). Figure 1d−f shows a schematic representation of the TSV filling process illustrating in yellow the expected organic impurities as a working hypothesis for our further investigations. To shine more light on this specific filling process, spatially resolved chemical analysis of the TSVs is required. In this contribution, we therefore introduce a novel approach for such chemical TSV analysis based on femtosecond laser ablation ionization mass spectrometry (fs-LIMS). This technique allows for direct analysis of micrometer-sized features[12−15] and 3D chemical elemental mapping of heterogeneous specimens.[16] To probe concentration gradients of impurities along the TSVs axis (side walls), a 1D LIMS depth profiling approach was applied (approach 1). For this purpose, systematic laser ablation studies were carried out to identify convenient experimental conditions for the TSV depth profiling. In the heterogeneous composed TSV target samples, the (metallic) polycrystalline Cu interconnect material is embedded into a single-crystalline (semiconductor) Si matrix (the wafer). Both components significantly differ in their physical properties (e.g., atomization energy, heat conductivity, reflectance, absorption coefficient, etc.) that are of relevance for the laser ablation process. A complementary approach that further quantifies the carbon (C) content inside the TSV was based on a LIMS surface analysis of filled TSVs that were cross-sectionally sliced along their main axis by mechanical polishing (approach 2). The results of both LIMS approaches are compared in this study with Scanning Auger Microscopy (SAM) data of a cross-sectioned TSV. This comparison allows for the exact localization of embedded organic impurities.

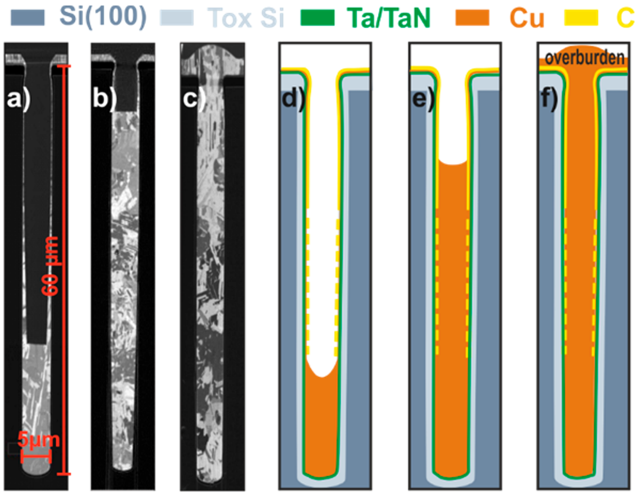

Figure 1. (a−c) SEM cross-sections of TSVs at different stages of the electro-plating process (prior to annealing). (d−f) Corresponding sketches illustrating the presence of expected organic impurities.

■ MATERIALS AND METHODS

Samples. Figure 2 presents top-view (panel a) and cross-sectional view (panel b) optical micrographs of a Cu TSV array embedded in a Si wafer (provided by BASF SE) studied herein. The 5 μm (diameter) × 50 μm (depth) Cu TSVs are embedded in a Si(100) matrix. TSVs and Si are separated from each other by a 650-nm-thick TOX/SiO_2 dielectric layer, a 25-nm-thick TaN/Ta diffusion barrier layer, and a 50-nm-thick Cu seed layer. Note that the bright spots in Figure 2a represent eroded TSVs that were already subject to LIMS depth profiling (approach 1) in contrast to the smaller, yellow dots that represent intact TSVs. The Cu overburden was removed prior to the LIMS depth profiling by means of local (*in situ*) laser ablation treatment or by (*ex situ*) mechanical polishing (Figure

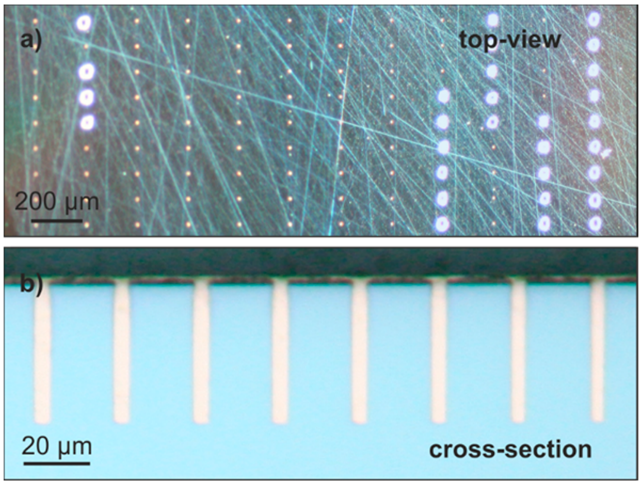

Figure 2. Optical microscope images of TSV arrays embedded in a Si wafer: (a) top-view and (b) cross-sectional view.

2a). TSV cross-sections (Figure 2b) were prepared by mechanical polishing (see below).

Polishing Procedure. For the mechanical polishing treatment, the wafer coupon samples were first embedded into a two-component epoxy (EpoFix hardener and resin cat. no. 40200029, Struers GmbH, Switzerland). The molds were then cured for ∼24 h at RT. Two sequential mechanical polishing steps using SiC foils (400/1200) were applied first to the wafer coupon/resin specimens using a commercial grinding machine (TEGRAMIN 20, Struers GmbH), followed by two diamond suspension polishing steps containing 3 and 1 μm diamond particles (DiaPro Dac 3 μm, 500 mL (40600371); DiaPro Nap B 1 μm, 500 mL (40600373), Struers GmbH, Switzerland). A commercial polishing cloth (MD/DP-Dur, Struers GmbH, Switzerland) served as a support.

Laser Ablation Ionization Mass Spectrometry (LIMS). The basic operation mode and the performance of the LIMS instrument used in this current study was already described in previous publications[17−22] and is therefore only briefly discussed in the following: The LIMS system consists of a miniature reflectron-type time-of-flight (R-TOF) mass analyzer (160 mm × ø 60 mm) that is coupled to a Ti-Sapphire laser system (CPA system, Clark-MXR Inc., USA) to promote ablation and ionization of the target material. The laser system operates at a wavelength of 775 nm and produces pulses with a width of ∼190 fs. Additional implementation of a beam shaper (Focal-πShaper, AdlOptica GmbH, Germany) in the beam delivery system converted the initial Gaussian pulse profile of the fs-laser system to a quasi-flat-top profile. Because fused silica is used for the optical parts in the shaper, changes in the group velocity dispersion are negligible at this pulse width. Each single laser pulse applied to the sample induced ablation and ionization of material and triggered the data acquisition cards to record a TOF spectrum. Two 12 bit high-speed digitizer PCIe cards (U5303A, Keysight, USA), each with two channels recording at 1.6 GSamples/s, were used for the measurements of single laser shots mass spectra at 1 kHz laser pulse repetition rate. A microchannel plate detector (MCP) system in chevron configuration was used for the detection of ions generated during the ablation/ionization process.[23] Only positively charged species can enter the mass analyzer and arrive at the detector system at time sequences proportional to the square root of their mass-to-charge ratio (TOF principle). The acquired time spectra were converted to mass spectra according to the relation $m(t) = k_0(t - t_0)^2$, where m denotes the mass in amu, t the arrival time (TOF) of isotopes detected in s, and k_0 and t_0 are internal calibration constants determined from the slope and the y-axis intercept of the linear regression of $\sqrt{m}$ versus t.[18] The intensity of each isotope was derived from a direct integration method using an adaptive Simpson quadrature integration of the mass peaks (in time domain) that are interpolated by a spline function.[22]

Measurement Procedure. *In situ Optical Microscopy.* An in-house fabricated optical microscope system was implemented in the LIMS instrumental setup for precise positioning of the μm-sized TSV structures below the mass analyzer. The optical system is equipped with a modified Nikon 10× objective with a numeric aperture (NA) of 0.3 with a spatial resolution of about 1 μm.

Study on the TSV Specific Laser Ablation Characteristics. The laser ablation process was studied on the TSVs by systematically varying the total number of laser shots and the laser pulse energies. Ablation craters were produced by 1500, 1000, 500, and 100 laser shots with pulse energies ranging from 2.4 μJ to 3.1 μJ (see Figure 4). All craters were analyzed by atomic force microscopy (AFM, Nanosurf FlexAFM V2 system, using Tap150Al-G silicon cantilevers) and high-resolution scanning electron microscopy (HR-SEM, field emission scanning electron microscope DSM 982 Gemini, Zeiss, Oberkochen, Germany).

Chemical Analysis of TSVs. Depth Profiling LIMS Analysis (Approach 1). Three types of TSV specimens were subject to the top-to-bottom depth profiling analysis differing in their specific treatment prior to the depth profiling. The *as received* samples still contained the Cu overburden (Figure S-2a). To avoid undesired (artificial) contributions of the Cu overburden to the Cu and C signals during the measurement, the overburden was removed in the vicinity of the TSVs, for instance, by an *ex situ* mechanical polishing treatment prior to the LIMS depth profiling (see above). Note that with this mechanical polishing, not only the Cu overburden is typically removed but unintentionally also the topmost part of the Cu TSV as the mechanical process cannot be stopped with high accuracy. An alternative for this overburden removal is an *in situ* laser ablation pretreatment. For this purpose, 30 high energetic (∼13 μJ) laser shots were concentrically applied around the TSV features (Figure S-2b).

For all depth profiling measurements, identical laser ablation conditions were applied. Each depth profile campaign consisted of 10 000 laser pulses in total with pulse energies of ∼2.5 μJ. Each resulting LIMS depth profile therefore consists of 10 000 individual data points extracted from the same number of single laser shot mass spectra. The applied experimental laser conditions were sufficient to ablate the entire TSV and to penetrate further into the Si matrix.

Cross-Sectional TSV Surface Analysis (Approach 2). In an alternative approach, TSVs were cross-sectioned by mechanical polishing and subsequently subjected to LIMS surface analysis particularly focusing on the opening (upper ∼33%) and the bottom (lower ∼33%) of the TSVs (see Figure 2b). To remove residuals and surface contaminations that might originate from the initial mechanical polishing treatment, the cross-sectioned TSVs were precleaned by a gentle *in situ* laser ablation treatment on each location of interest by applying 30 000 laser pulses at particularly low energies of ∼0.6 μJ. For the subsequent chemical analysis, another 30 000 laser shots with the same pulse energy were applied on the afore cleaned locations of the cross-sectioned TSVs.

Cross-Sectional Analysis of LIMS Craters. *Lithography and Selective Anisotropic Etching of Si.* For the characterization of the crater depths and morphologies induced by the laser ablation process, LIMS craters were cross-sectioned by a combination of lithographic and deep reactive ion etching (DRIE) methods. A patterned polymer mask (AZ4533 resist, spin-coated at 4000 rpm to yield a 3.3 μm thick film, backing at 110 °C on a hot-plate for 60 s, AZ developer to release exposed areas) was deposited on top of the wafer coupon surface in such a way that one-half of the depth-profiled TSV row was covered by the protecting polymer film. The unprotected areas of the Si substrate were then exposed to multiple cycles of a selective Si etching (not affecting the TSV's Cu body) using sulfur hexafluoride [SF_6] plasma (Alcatel 1800 W, etch rate of 5 μm/min) for the Si removal. Each Si etch step was followed by the deposition of a chemically inert passivation layer (Teflon) to further promote the anisotropic Si etching. After removal of the resist in acetone and cleaning in isopropanol, the cross-

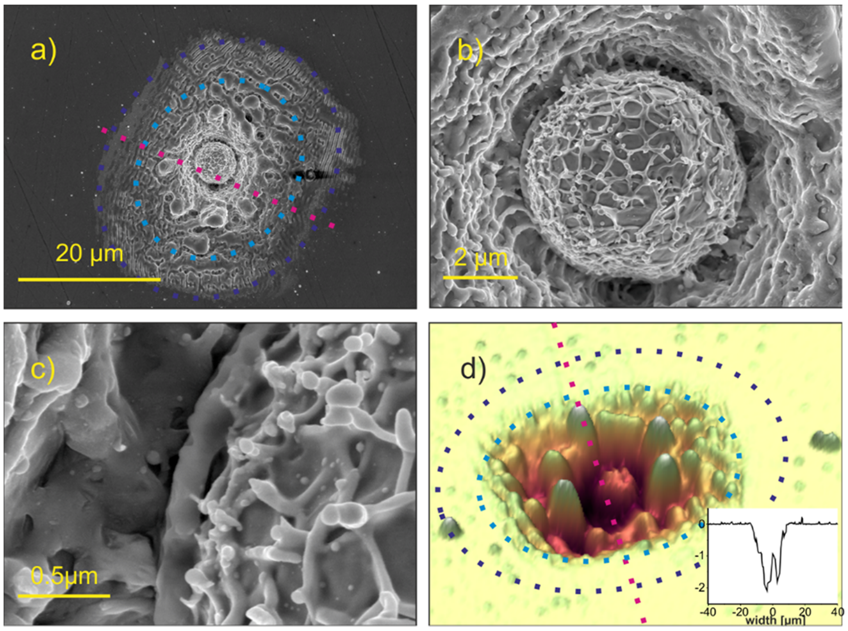

Figure 3. (a−c) HR-SEM top-view images of a crater formed on a TSV by applying 100 consecutive laser shots with ∼3.0 μJ/pulse. (d) 3D AFM scan of the crater's topmost section. Inset image of panel d presents the corresponding cross-sectional depth profile along the scan line (indicated by the purple dotted line) revealing a higher Cu core inside the crater. The light blue dotted line indicates the actual crater, and the dark blue dotted line shows the boarder of the affected area where no significant ablation occurred.

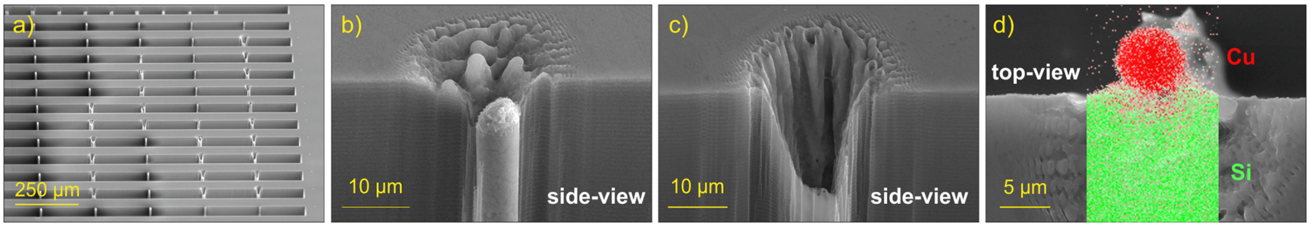

Figure 4. (a) SEM overview of the TSV crater cross-sections obtained by selective etching of Si (Bosch process). The energy and number of applied laser pulses were 2.4−3.1 μJ and 100−1500, respectively. (b) Close-up of a crater cross-section formed by 100 laser shots at ∼3.0 μJ/pulse. (c) Close-up of a crater cross-section formed by 1000 laser shots at ∼3.1 μJ/pulse. (d) Top-view SEM/2D-EDX (energy-dispersive X-ray spectroscopy, Noran SIX NSS200 EDX spectrometer) measurement of the crater presented in b.

sectioned ablated craters were analyzed by tilted SEM imaging (Hitachi S-3000N Scanning Electron Microscope (Japan), accelerating voltage of 25 kV at a working distance of 10 mm).

■ RESULTS AND DISCUSSION

Top-down and Cross-Sectional Crater Analysis. Figure 3 presents top-view HR-SEM images (panels a−c) and AFM analysis (panel d) of the initial stage of LIMS crater formation after applying 100 laser shots on an isolated TSV feature at a pulse energy of ∼3.0 μJ. Clearly visible are several concentric, almost-circular zones surrounding the TSV center. The outermost area affected by the laser beam (indicated by dark blue dotted lines) is characterized by severe morphological changes of the Si substrate as consequence of local melting and subsequent solidifying processes without any significant net erosion of Si material.[24] The observed SEM ripples in the substrate are well-known morphological features which appear on the Si upon laser irradiation even below the material-specific ablation threshold.[25−27] They are however not visible in Figure 3d due to the significantly larger topography of the ablated crater.

Note that the damage of the laser pulse on the target substrate is significantly reduced in the peripheral zones as compared to the center of the laser impact where the actual material ablation takes place. The LIMS crater itself, indicated by the light blue dotted line (Figure 3a), can be subdivided into two subzones: The inner one relates to the Cu TSV core, whereas the outer crater zone belongs to the ablated Si matrix (panel b). This assignment is confirmed by 2D top-view EDX mapping of cross-sectioned TSVs (see Figure 4d). A corresponding side-view representation of the 2D EDX map of the cross-sectioned TSV feature presented in Figure 4d is provided in the SI. Note that the crater dimension clearly exceeds the diameter of the Cu TSV of 5 μm so that the Cu and the surrounding Si matrix are both affected by the LIMS crater evolution. Interestingly, there is a characteristic recess/depression separating the Cu TSV from the Si matrix inside the LIMS crater thus pointing to a local nonuniform removal of material during the ablation process (Figure 3b). Obviously, the Ta/TaN/SiO_2 interface separating the Cu TSV from the Si matrix gets preferentially eroded upon laser irradiation (see Figures 3b,c and 4b). Such a slight nonuniformity in the material removal becomes more obvious by the top-surface AFM image and line-scan across the TSV center clearly showing a spike in the center (Figure 3d), distinctly separated from the surroundings and not being artificially created by the tip's convolution. The hemispherical shape of the outermost part of the Cu via inside the LIMS crater in combination with the appearance of randomly oriented nanoripples on its surface is indicative for a transient melting of the Cu surface during the laser ablation process (Figure 3b). Also note that the morphology of the (Si) crater side wall (Figure 3b) significantly deviates from comparable LIMS craters formed in the pure Si matrix (see Figure S-5). These observations are indicative for laser ablation and crater evolution processes that are distinctly different for the homogeneous single-component Si substrate and compared to the highly heterogeneous multicomponent Si/Ta/TaN/SiO_2/Cu system studied herein. In particular the interaction of the crater side walls with the plasma plume formed inside the crater strongly depends on the specific chemical composition of the heterogeneous target system that is subjected to the laser irradiation.[28,29] It is the ablation of Cu inside the LIMS crater which particularly facilitates the formation of ionic species of higher charge state, e.g., Si^{4+} and Si^{3+} (see Figure S-3), thus being indicative for a significantly higher plasma temperature inside the crater as compared to ablation processes in the pure Si (see SI file). The elevated plasma temperature inside the TSV crater is most likely also the physical origin for the prominent melting/resolidifying effects observed in the top-down SEM inspection of Figure 3.[28]

In order to systematically investigate profiles and depths of laser ablation craters on individual TSV features, a 2D array of craters was ablated on a test Si wafer coupon comprising TSVs. Herein, laser pulse energy and number of applied laser pulses were varied from 2.4 to 3.1 μJ, respectively, from 100 to 1000. For the cross-sectioning of the thus obtained ablation craters, we applied a selective anisotropic etching process to the entire TSV wafer coupon. Note that here only the Si is affected by the chemical etching process, leaving the Cu TSV body almost intact (thermal load may change its shape slightly). Figure 4a shows a survey SEM image of the cross-sectioned craters which were then individually inspected by SEM analysis. Representative examples are given in Figure 4 demonstrating an initial (100 laser shots, panel b) and an advanced stage (1000 laser shots, panel c) of the crater evolution process. Note that due to the Si-selective etching, the remaining Cu via might slightly protrude from the etched Si matrix (see also panel b (cross-section) and d (top-view) of Figure 4). A detailed analysis of the cross-sectioned LIMS craters in Figure 4 yields (i) a correlation between the applied laser pulse energies and the resulting mean ablation rates (Figure 5, panel a) and (ii) a correlation between the total number of applied laser pulses and the resulting crater depths (Figure 5, panel b). For comparison purposes, corresponding data from polycrystalline Cu and single-crystalline Si(100) were included into both graphs of Figure 5. The reported results show a qualitative trend. For the quantitative determination of the actual ablation rate, a statistically relevant number of measurement repetitions is required. Among these samples, it is the polycrystalline Cu which shows the highest ablation threshold for the laser ablation process which can be rationalized by its higher reflectance (R_{Cu} = 0.96, R_{Si} = 0.33).[30] For guidance, see the intersection of the (dotted) trend lines in Figure 5a with the x-axis. Once the damage threshold is reached, Cu shows the steepest increase in the mean ablation rate as a function of the pulse energy. This observation can be rationalized by the higher absorption coefficient of Cu ($\alpha_{Cu} = 7.89 \times 10^5$ cm^{-1}, $\alpha_{Si} = 0.01 \times 10^5$ cm^{-1})[30] in combination with a lower atomization energy as compared to Si (Cu: 337.4 kJ mol^{-1}; Si: 450 kJ mol^{-1}).[31] In agreement with this argumentation, we observe crater depths which evolve much faster with increasing number of applied laser pulses in the case of polycrystalline Cu as compared to Si (Figure 5, panel b). Interestingly, the crater depth development reaches in all cases a characteristic material-specific plateau which is highest for Cu (above 50 μm depth). This saturation may emerge as the laser irradiance decreases with increasing depth and hence is not sufficient anymore to induce material dependent ablation. The heterogeneous TSV sample composition (Si/Ta/TaN/SiO_2/Cu) shows overall laser ablation characteristics which are located somewhere between the ones of polycrystalline Cu and crystalline Si, respectively. An important finding of our systematic study, however, is that the crater evolution of these heterogeneous TSVs is more uniform than expected from the rather different ablation characteristics of the pure Cu and Si reference samples. In particular, we do not observe a substantially higher removal of Cu from the TSV body during the laser ablation process compared to Si. As discussed above, this effect can most likely be attributed to an increased Si ablation rate that gets significantly higher in the presence of Cu in terms of a "Cu-assisted" Si ablation. To the best of our knowledge, this is the first time that such a "synergistic" ablation effect is reported for heterogeneous multicomponent systems where the individual components substantially differ in their ablation characteristics.

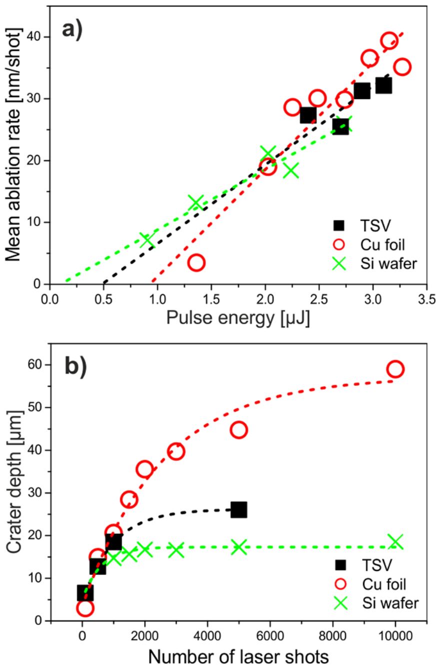

Figure 5. (a) Energy-dependence of mean ablation rates, derived from 500 laser shots for the TSV, polycrystalline Cu foil, and single-crystalline Si(100) wafer. (b) Ablation depths of craters formed on TSV sample, polycrystalline Cu foil, and conventional Si(100) wafer for various number of laser shots at ~2.7 μJ/pulse energy.

Depth Profiling LIMS Analysis (Approach 1). Figure 6 shows a representative LIMS depth profile of a single TSV where the overburden has been removed by mechanical polishing. Removal of this layer is a crucial prerequisite to avoid undesired contributions from the overburden to the LIMS depth profile of the TSV (see Figure S-2).[14] However, the applied mechanical polishing procedure did not solely remove the overburden but also the upper part of the TSV

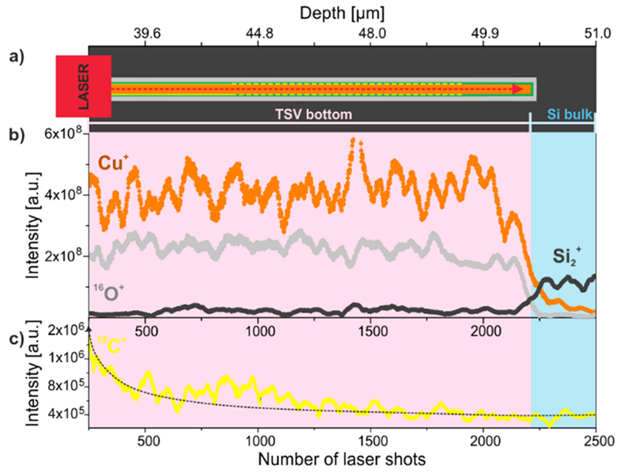

Figure 6. Chemical depth profile of an overburden-free (mechanically polished) TSV. (a) Representation of the TSV bottom illustrating approach 1. (b) Depth profile of Cu$^+$, ^{16}O$^+$, and Si$_2$$^+$. (c) Depth profile of ^{12}C$^+$ inside the TSV feature. For all depth profiles a Savitzky−Golay filter (100 points averaged, second order polynomial) was used.

structure (determined from cross-sectional SEM imaging). The applied laser pulse energy of ∼2.5 μJ (determined from systematic laser ablation studies) was sufficiently high to ensure constant ablation and stable signal intensity at the expense, however, of the resulting mass resolution. The energy of 2.5 μJ showed the best results among the tested pulse energies, which allowed for complete and uniform drilling through the TSV feature applying a reasonable number of laser shots that results in a reasonable depth resolution of the chemical profile. A poor mass resolution was found in particular for Cu and Si due to charging effects. We therefore integrated the corresponding signals over the entire range of isotopes (for Cu$^+$, 63, 65; for Si$_2$$^+$, 56−58). Charged Si dimer clusters (Si$_2$$^+$) thereby served as tracers for the TSV depth profiling. The corresponding signals of the singly charged Si$^+$ isotope could not be used for this purpose since they severely suffer from saturation effects and the overlapping in the mass spectra with signals of the doubly charged Cu^{2+} ions. The mass resolution for C and O species was sufficiently high to allow for an accurate integration of the respective ^{12}C$^+$ and ^{16}O$^+$ isotope signals. However, the accurate quantification of these elements cannot be provided as Si and Cu are not sufficiently resolved under these measurement conditions.

Figure 6b demonstrates that the intensities of the ^{16}O$^+$ and the Cu$^+$ signals almost vanish in the LIMS depth profile after ∼2 000 laser shots, indicating that the bottom of the TSV feature was reached. The chemical origin of the ^{16}O$^+$ species is the SiO$_2$ (TOX) of the barrier layer separating the Cu via from the surrounding Si matrix. This explains why the ^{16}O$^+$ and the Cu$^+$ signals are strongly correlated with each other. The corresponding Si$_2$$^+$ depth profile is clearly anticorrelated to the intensity trends of the ^{16}O$^+$ and the Cu$^+$ signals and strongly increases when reaching the TSV bottom. Note that the nature of the Si species that are detected in the mass spectra during the depth profiling fundamentally changes after passing the bottom of the TSV. Whereas multiply charged but monomeric Si species are dominant in the respective mass spectra during the TSV depth profiling, we observe a clear preference toward singly charged Si and Si clusters (e.g., Si_2^+, Si_3^+, and Si_4^+) when the depth profiling extends into the Si matrix after passing the via bottom. This intriguing finding is also supporting our claim of a plasma whose temperature inside the ablation crater crucially depends on the ablated material. Obviously, there is a clear transition from “hot plasma” (heterogeneous TSV) toward “cool plasma” conditions (pure Si) when passing the TSV bottom and further penetrating into the bulk of the Si substrate (see Figure S-3). Our ablation investigations (Figure 5) enabled the correlation of in a first approximation the applied number of shots in the depth profile to an absolute depth scale (see uper *x*-axis in Figure 6) by using the exponational trend derived from the TSV measurements in Figure 5b.

Contrary to the abrupt intensity trends observed for the major elements Si and Cu, we observe a continuous decrease (down to ∼7% of the initial signal intensity) of the ^{12}C$^+$ signal in the respective depth profile (see Figure 6c). The chemical origin of these ^{12}C$^+$ species are most likely the (polymeric) organic contaminants preferentially embedded at the side walls of the TSV. Our experimental observation of a C gradient in the TSV depth profile supports our initial hypothesis of a suppressor film which is more compact, thicker, and therefore more effective at the feature opening during the bottom-up fill than at the TSV bottom (see Figure 1). However, the excess structure removal during the mechanical polishing did not allow for the 1D depth profiling analysis of C at the feature opening. Following the measured concentration trend, an even more pronounced gradient is expected to be observed if the entire TSV structure is considered. The applied laser ablation conditions did not allow for an accurate quantitative determination of the C content. The conditions for the laser ablation depth profiling process (pulse energy of ∼2.5 μJ) yielded a poor mass resolution. Therefore, an alternative LIMS approach was developed based on a surface analysis of TSV features that were cross-sectioned by mechanical polishing prior to the analysis (approach 2).

Cross-Sectional TSV Surface Analysis (Approach 2). Figure 7b shows such a cross-sectioned TSV after the LIMS analysis that was particularly focusing on the via opening and its bottom. For this analysis, gentle laser ablation conditions at reduced pulse energies of ∼0.6 μJ were applied, thus resulting

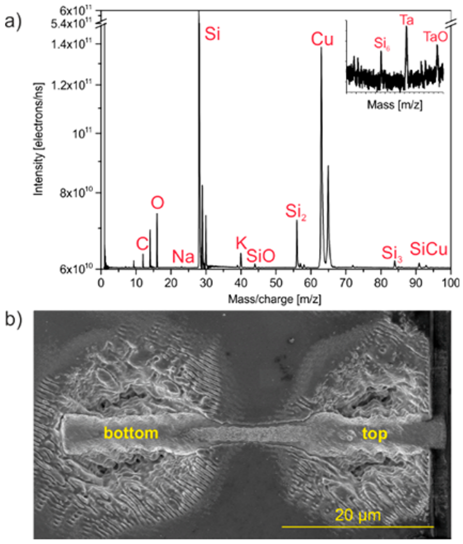

Figure 7. (a) Typical mass spectrum obtained from the surface analysis. (b) SEM image of the cross-section of a TSV feature showing the analyzed areas on the two extremities of the Cu channel.

in a significantly improved mass resolution that even allowed for the detection of Ta in the barrier layer (see inset in Figure 7a). In total, four adjacent TSVs were considered for the quantification of the C/Cu ratios (w%) that were derived from an integration of the respective $^{12}C^+/Cu^+$ peaks in the accumulated mass spectra (see Figure 7a) and considering a calibration factor calculated from a C containing Cu certified reference sample (see SI for measurement details). Each measurement consisted of 60 000 laser pulses, whereas only the last 30 000 were considered for the analysis to avoid surface contaminants induced by the sample handling. The 3D microscopy analysis of the laser affected zone revealed a removal of ~350 nm Cu. Assuming a constant ablation rate, the pretreatment of the sample surface by means of 30 000 laser shots induced a material removal of about 175 nm. Further information about the laser-induced craters on these cross-sectional TSVs is provided in the SI.

Our surface analysis revealed mean C/Cu ratios of 0.008 ± 0.002 and 0.012 ± 0.002 for the via bottom and the via opening, respectively. This corresponds to a C content which is higher by a factor of ~1.5 at the feature opening (average value of the upper ~33%) as compared to the bottom section. Note that the lateral spatial resolution of the LIMS analysis is, however, not sufficient to discriminate between impurities embedded into the interior of the Cu via and residuals of the polymeric suppressor films that were preferentially accumulated and overgrown at the feature side walls during the bottom-up fill.

Scanning Auger Microscopy (SAM). To localize the C contents in the TSV, we therefore applied, in addition, Scanning Auger Microscopy (SAM) to the cross-sectioned TSVs. From the combined SEM and SAM images presented in Figure 8, we can conclude that the majority of the C impurities is indeed preferentially localized at the feature side walls. Note that we restrict ourselves in demonstrating the relative differences in the C contents at the interface/side walls and the TSV interior. Due to possible further accumulation of C impurities upon extended SEM/SAM analysis, we do not provide any quantification of the C content at this point. These results are in full agreement with the initial working claim of an overgrown polymeric suppressor film located at the TSV side walls. Furthermore, the particularly low C content inside the TSV is most likely the chemical origin for the well-crystallized Cu inside the via (Figure 1).

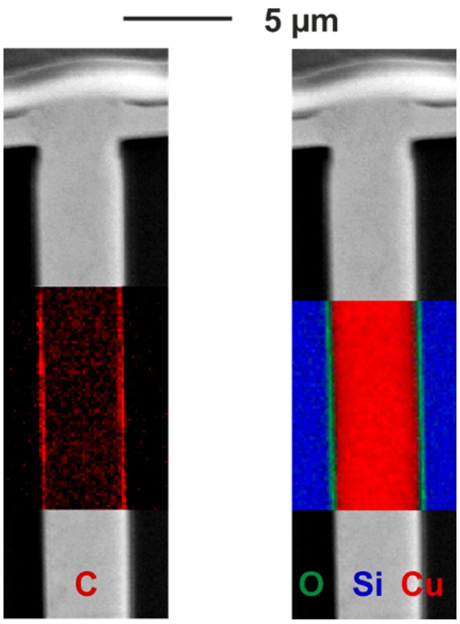

Figure 8. Cross-sectional SEM and superimposed local SAM for qualitative C, O, Si, and Cu determination.

■ CONCLUSION

In this contribution, we presented a combined LIMS/SAM study on the additive embedment into TSV, which occurs during the additive-assisted electrodeposition of Cu into these features. The LIMS investigations in combination with the cross-sectional SAM analysis could indeed verify a mechanistic detail of the specific TSV fill process. Polymeric additives are embedded preferentially at the feature side walls during the bottom-up fill. A gradient in the $^{12}C^+$ depth profile is indicative of a well-developed and effective polymeric suppressor film at the via opening. The interior of the Cu via remains, by contrast, largely contamination-free, thus also explaining the fast recrystallization of the Cu inside the TSV even at room temperature as evidenced by cross-sectional SEM analysis.

The laser ablation depth profiling of these highly heterogeneous TSV features proceeded more uniformly than expected from the rather different ablation characteristics of pure Si and Cu. This intriguing observation was rationalized on the basis of a particular synergistic effect in terms of a Cu-assisted ablation of Si.

In addition, a novel preparation approach was used to study in detail the LIMS crater evolution on these highly heterogeneous TSV features. Combination of lithographic and selective Si ion etching methods to arrays of LIMS craters allowed for their fast cross-sectioning as a basis for a systematic HR-SEM analysis.

■ ASSOCIATED CONTENT

Supporting Information

The Supporting Information is available free of charge on the ACS Publications website at DOI: 10.1021/acs.analchem.7b05313.

> Overview on the classical concept of Damascene plating and of all applied depth profiling approaches, illustration of multiple-charged and cluster signal evolution, scheme of crater cross-sectional procedure, surveys of Si and Cu craters, side-view representation of the 2D EDX map, description of reference measurement, 3D optical white light microscope image (PDF)

■ AUTHOR INFORMATION

Corresponding Authors

*E-mail: valentine.grimaudo@dcb.unibe.ch. Phone: +41 31 631 43 17.

*E-mail: peter.broekmann@dcb.unibe.ch. Phone: +41 31 631 43 17.

ORCID

Valentine Grimaudo: 0000-0002-7010-5903
Pavel Moreno-García: 0000-0002-6827-787X
Andreas Riedo: 0000-0001-9007-5791
Peter Wurz: 0000-0002-2603-1169
Peter Broekmann: 0000-0002-6287-1042

Author Contributions

The manuscript was written through contributions of all authors. All authors have given approval to the final version of the manuscript.

Notes

The authors declare no competing financial interest.

■ ACKNOWLEDGMENTS

We acknowledge the work from the technical staff of the Department of Chemistry and Biochemistry and of the Space Research and Planetary Sciences division at the University of Bern, Switzerland. Further, we highly appreciate the support by the IBM's BRNC technical staff, and we gratefully acknowledge the wafer supply by BASF SE, as well as the performed SAM measurements at the MPIE (Düsseldorf, Germany). This study was additionally performed with the support of the interfaculty Microscopy Imaging Centre (MIC) of the University of Bern, Switzerland. This work was funded by the Swiss National Science Foundation (SNSF).

■ REFERENCES

(1) Moore, G. E. *IEEE Solid-State Circuits Newsletter* **2006**, *11*, 33−35.

(2) Hamdioui, N. Z. H. a. S. In *2008 3rd International Design and Test Workshop*, Monastir, Tunisia, 2008; Institute of Electrical and Electronics Engineers, 2008; pp 98−103.

(3) Garrou, P.; Ramm, P.; Koyanagi, M. In *Handbook of 3D Integration*; Wiley-VCH Verlag GmbH & Co. KGaA, 2014; pp 1−12.

(4) Gagnard, X.; Mourier, T. *Microelectron. Eng.* **2010**, *87*, 470−476.

(5) Gambino, J. P.; Adderly, S. A.; Knickerbocker, J. U. *Microelectron. Eng.* **2015**, *135*, 73−106.

(6) Shen, W.-W.; Chen, K.-N. *Nanoscale Res. Lett.* **2017**, *12*, 56.

(7) Hoang, V. H.; Kondo, K. *Electrochim. Acta* **2016**, *212*, 270−276.

(8) Akolkar, R. *ECS Electrochem. Lett.* **2013**, *2*, D5−D8.

(9) Radisic, A.; Lühn, O.; Vaes, J.; Armini, S.; El-Mekki, Z.; Radisic, D.; Ruythooren, W.; Vereecken, P. M. *ECS Trans.* **2010**, *25*, 119−125.

(10) Lühn, O.; Radisic, A.; Vereecken, P. M.; Van Hoof, C.; Ruythooren, W.; Celis, J. P. *Electrochem. Solid-State Lett.* **2009**, *12*, D39−D41.

(11) Lühn, O.; Van Hoof, C.; Ruythooren, W.; Celis, J. P. *Electrochim. Acta* **2009**, *54*, 2504−2508.

(12) Tulej, M.; Neubeck, A.; Ivarsson, M.; Riedo, A.; Neuland, M. B.; Meyer, S.; Wurz, P. *Astrobiology* **2015**, *15*, 669−682.

(13) Riedo, A.; Grimaudo, V.; Moreno-García, P.; Neuland, M. B.; Tulej, M.; Wurz, P.; Broekmann, P. *J. Anal. At. Spectrom.* **2015**, *30*, 2371−2374.

(14) Cedeño López, A.; Grimaudo, V.; Moreno-García, P.; Riedo, A.; Tulej, M.; Wiesendanger, R.; Wurz, P.; Broekmann, P. *J. Anal. At. Spectrom.* **2018**, *33*, 283−293.

(15) Wiesendanger, R.; Grimaudo, V.; Moreno-Garcìa, P.; Cedeñod Lopez, A.; Riedo, A.; Tulej, M.; Wacey, D.; Wurz, P.; Sheac, H. *Astrobiology* **2018**, DOI: 10.1089/ast.2017.1780, in press.

(16) Grimaudo, V.; Moreno-García, P.; Riedo, A.; Meyer, S.; Tulej, M.; Neuland, M. B.; Mohos, M.; Gütz, C.; Waldvogel, S. R.; Wurz, P.; Broekmann, P. *Anal. Chem.* **2017**, *89*, 1632−1641.

(17) Tulej, M.; Riedo, A.; Iakovleva, M.; Wurz, P. *Int. J. Spectrosc.* **2012**, *2012*, 1.

(18) Riedo, A.; Bieler, A.; Neuland, M.; Tulej, M.; Wurz, P. *J. Mass Spectrom.* **2013**, *48*, 1−15.

(19) Riedo, A.; Meyer, S.; Heredia, B.; Neuland, M. B.; Bieler, A.; Tulej, M.; Leya, I.; Iakovleva, M.; Mezger, K.; Wurz, P. *Planet. Space Sci.* **2013**, *87*, 1−13.

(20) Riedo, A.; Neuland, M.; Meyer, S.; Tulej, M.; Wurz, P. *J. Anal. At. Spectrom.* **2013**, *28*, 1256−1269.

(21) Bieler, A.; Altwegg, K.; Hofer, L.; Jäckel, A.; Riedo, A.; Sémon, T.; Wahlström, P.; Wurz, P. *J. Mass Spectrom.* **2011**, *46*, 1143−1151.

(22) Meyer, S.; Riedo, A.; Neuland, M. B.; Tulej, M.; Wurz, P. *J. Mass Spectrom.* **2017**, *52*, 580−590.

(23) Riedo, A.; Tulej, M.; Rohner, U.; Wurz, P. *Rev. Sci. Instrum.* **2017**, *88*, 045114.

(24) Rethfeld, B.; Ivanov, D. S.; Garcia, M. E.; Anisimov, S. I. *J. Phys. D: Appl. Phys.* **2017**, *50*, 193001.

(25) Costache, F.; Kouteva-Arguirova, S.; Reif, J. *Appl. Phys. A: Mater. Sci. Process.* **2004**, *79*, 1429−1432.

(26) Bonse, J.; Rosenfeld, A.; Krüger, J. *J. Appl. Phys.* **2009**, *106*, 104910.

(27) Abere, M. J.; Zhong, M.; Krüger, J.; Bonse, J. *MRS Bull.* **2016**, *41*, 969−974.

(28) Eggins, S. M.; Kinsley, L. P. J.; Shelley, J. M. G. *Appl. Surf. Sci.* **1998**, *127*, 278−286.

(29) Borisov, O. V.; Mao, X.; Russo, R. E. *Spectrochim. Acta, Part B* **2000**, *55*, 1693−1704.

(30) Johnson, P. B.; Christy, R. W. *Phys. Rev. B* **1972**, *6*, 4370−4379.

(31) Lide, D. R. *CRC Handbook of Chemistry and Physics*, 84 ed.; CRC Press: New York, 2003−2004.